

A full-chip 3D computational lithography framework

Peng Liu*, Zhengfan Zhang, Song Lan, Qian Zhao, Mu Feng,
Hua-yu Liu, Venu Vellanki, Yen-wen Lu

Brion Technologies, Inc., an ASML company, 4211 Burton Drive, Santa Clara, CA, USA 95054

ABSTRACT

3D lithography simulations capable of modeling 3D effects in all lithographic processes are becoming critical in OPC and verification applications as semiconductor feature sizes continue to shrink. These effects include mask topography, resist profile and wafer topography. In this work we present an efficient computational framework for full-chip 3D lithography simulations. Since fast modeling of mask topography effects has been studied for many years and is a relatively mature area, we will only briefly review a full-chip 3D mask model, Tachyon M3D, to highlight the importance and modeling requirements for accurate prediction of best focus variations among different device features induced by mask topography. We will focus our discussions on a full-chip 3D resist model, Tachyon R3D, its derivation and simplification from a full physical resist model. The resulting model form is fully compatible with the existing 2D resist model with added capabilities for resist profile and top loss prediction. A benchmark against the full physical model will be presented as well. We will also describe the development of a full-chip 3D wafer topography model, Tachyon W3D, and the preliminary results against rigorous simulations.

Keywords: 3D lithography, mask topography, EMF, resist model, resist profile, resist loss, wafer topography.

1. INTRODUCTION

As semiconductor feature sizes continue to shrink, the allowable error margins for critical dimension (CD) control become increasingly tight. As a result, 3D lithography effects previously considered trivial start to show bigger impact to device patterning processes. These effects include mask topography, resist profile and wafer topography.

Mask topography effects have already generated a lot of studies since the minimum feature size on mask reduced to below the exposure wavelength. These studies have shown that some important experimental observations cannot be explained by thin mask model (a.k.a. Kirchhoff model). Examples of these observations include image imbalance in earlier development of alternating phase shift mask [1-2] and more recently best focus variations among different device features [3-5]. These observations can only be explained by the electromagnetic field (EMF) scattering effects caused by the mask topography.

Device makers also begin to observe resist profile related patterning issues, for example, effects of resist top loss and sidewall angle on the subsequent etch process and printing problems of sub-resolution assist features (SRAF). Standard full-chip optical proximity correction (OPC) and verification applications generally compute only 2D resist contours in a given horizontal resist plane. However, it has been shown that 3D resist simulations are required to identify those patterning problems that are impossible to detect with 2D contours [6-7].

Lastly, wafer topography effects from underlying patterned layers begin to receive attentions as well, particularly for patterning layers where no or less effective bottom anti-reflection coatings (BARC) are used. Both experimental studies and rigorous 3D wafer simulations have shown that the exposure image distortions caused by the underlying wafer topography are so severe for some features in an implant patterning process that OPC is required to correct the problem [8]. Wafer topography effects in double-patterning processes have also been reported [9].

In order to detect and mitigate the problems related to 3D lithography effects via OPC at the mask data preparation stage, the associated computational lithography model must have the capability to accurately simulate these effects. Although rigorous physical models are available for accurate simulation of these effects, they are computationally too expensive to use in full-chip OPC and verification applications. In this work, we will describe a 3D computational lithography framework for full-chip applications.

*peng.liu@brion.com, 1-408-200-0843

In Section 2 we will, for completeness, briefly review our previous work on a full-chip 3D mask model, Tachyon M3D, and highlight the importance and modeling requirements for accurate prediction of best focus variations among different device features induced by mask topography. Then, in Section 3, we will describe the development of a full-chip 3D resist model, Tachyon R3D. Its derivation and simplification from a full physical resist model will be discussed in details. The benchmark against the full physical model will be presented as well. In Section 4 we will show the development work of a full-chip 3D wafer topography model, Tachyon W3D, and the preliminary results against rigorous simulations. Summary of this work is given in Section 5.

2. M3D

2.1 3D mask modeling requirements

Mask topography effects have been observed since the minimum feature size on mask reduced to below the exposure wavelength. An example of these effects is the image imbalance between 0- and 180-degree phase features observed many years ago in the development of alternating phase shift masks [1-2]. Recently, best focus variations among different device features have caught a lot of attention and the origin has been traced to mask topography as well [3-5].

In our previous work [5], we have shown that, for dense 1D line/space patterns under dipole illumination, the best focus is proportional to the phase difference between 0th and 1st diffraction orders. While thin mask model predicts zero phase difference and therefore zero best focus shift for masks such as chrome binary and attenuated phase shift masks, rigorous mask simulations show that the phase difference is not zero and is pattern dependent, leading to pattern-dependent best focus variation. The rigorous simulations also show that the phase difference varies significantly as a function of incident angle. These findings conclude that Kirchhoff approximation of thin mask model and Hopkins model of oblique incidence are no longer valid. A more rigorous treatment of mask EMF scattering effects and oblique incidence effects is required in order to accurately predict best focus variations. Although the above analysis is based on dense 1D line/space patterns, the conclusion should apply to 2D patterns as well.

2.2 M3D model

Tachyon M3D is a fast, approximate 3D mask model developed for full-chip OPC and verification applications. The details on its derivation are given in our previous work [5, 10]. In a nutshell, the mask transmitted field is computed by applying a set of M3D filters to the corresponding mask layout elements as illustrated in Figure 1. These elements include polygon area, edges and corners.

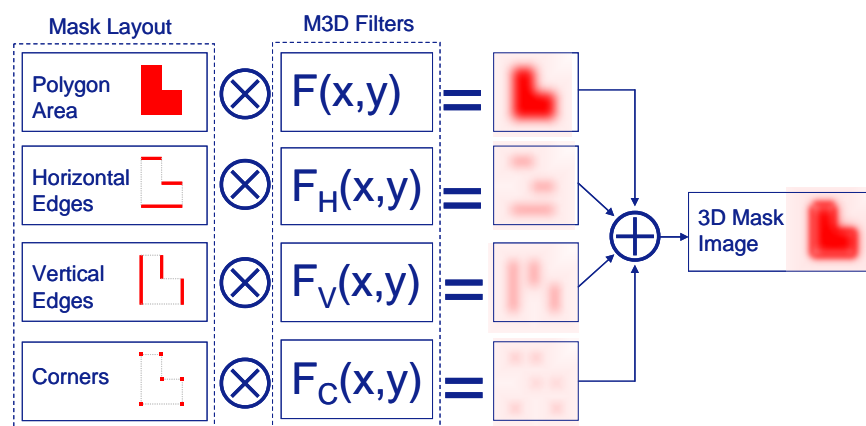


Fig. 1. Rendering of mask transmitted field in M3D model

In order to meet the modeling requirements described in Section 2.1, we have implemented the following features in the M3D model. (a) The M3D filters are extracted from the rigorous transmitted fields of the representative layout elements, which are computed using a rigorous EMF method that solves Maxwell's equations. As a result, the mask transmitted field rendered by M3D filters is more rigorous than that of Kirchhoff approximation. (b) The rigorous simulations in (a) are carried out on an array of incident angles and are later combined based on the actual illumination shape and

polarization to compute the corresponding M3D filters, as illustrated in Figure 2, which provides a more rigorous treatment of oblique incidence effects than Hopkins model.

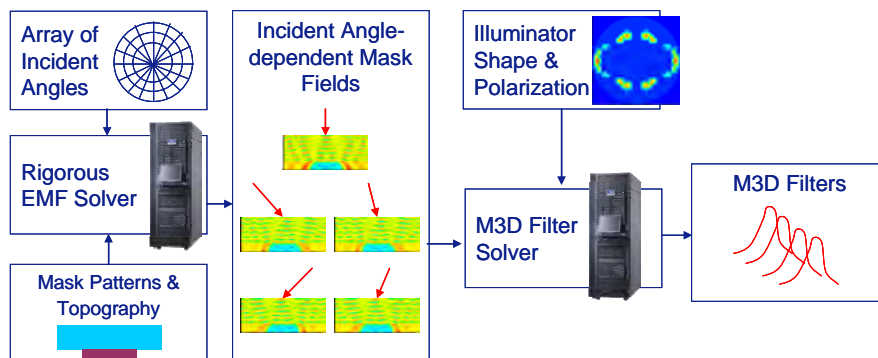


Fig. 2. Calculation of M3D filters

2.3 Accuracy validation

The above M3D features enabled the accurate prediction of best focus variations among different device features. An example is shown in Figure 3. More extensive benchmark studies of M3D against experiments and rigorous simulations can be found in our previous work [5, 10].

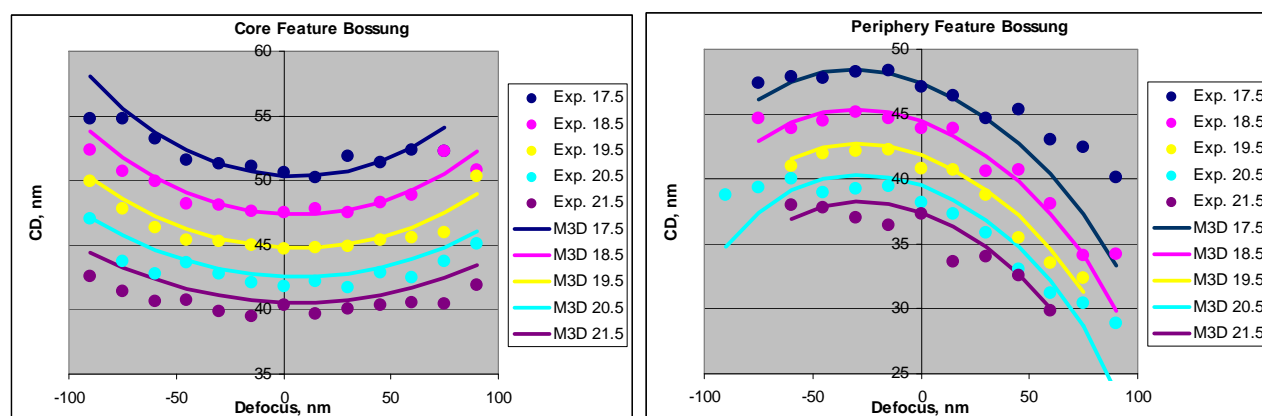


Fig. 3. Comparison of Bossung curves between M3D and experiment of different features on a Flash device where the core feature and the periphery feature have different best focus

3. R3D

3.1 State of the art

Standard OPC and verification applications are generally based on compact 2D resist models. The input to such a model is a 2D optical image sampled in a single plane, usually near the bottom of the resist. Various operations (e.g., 2D Gaussian blur, threshold, etc...) are applied to this image to mimic the resist processes. The final output of these operations is a 2D resist contour in that plane.

However, the resist contour in a single plane provides no information about resist 3D profile and top loss that can cause problems in the subsequent etch process. Recently studies have showed that these potentially catastrophic failures are predicted by a 3D physical resist model while the 2D model shows no issues [6-7]. These studies indicate that 3D resist models are required in OPC and verification applications in order to detect and correct the problems at the design stage.

While 3D physical resist models have been available for many years [11-13]. They are computationally too expensive for full-chip applications and are therefore generally found only in small-scale lithography simulators. In the following sub sections, we will formulate a full-chip 3D resist model, Tachyon R3D, which is derived and simplified from a 3D physical resist model.

3.2 A 3D physical resist model

In this work we choose the following 3D physical resist model of chemically amplified resists (CAR) as the starting point to formulate our full-chip 3D resist model.

3.2.1 Exposure model

In a chemically amplified resist, initial acid is produced during resist exposure. This process may be modeled by the following equations.

$$\frac{\partial[PAG]}{\partial t} = -C \cdot I \cdot [PAG] \quad (1.1)$$

$$[H] = 1 - [PAG] \quad (1.2)$$

where PAG is the photo-acid generator, I is the optical image in resist, C is the Dill's parameter related to photospeed of the resist [17], H is the acid, and [...] denotes the normalized concentration of the corresponding chemical specie.

3.2.2 Post-exposure bake (PEB) model

After exposure the resist is baked in which de-protection of inhibitors takes place to make the resist soluble. It is a complex process involving diffusion and reaction among acid, base and inhibitors. These processes may be modeled as follows.

$$\frac{\partial[M]}{\partial t} = -k_a \cdot [H] \cdot [M] \quad (2.1)$$

$$\frac{\partial[H]}{\partial t} = -k_Q \cdot [Q] \cdot [H] + D_H \nabla^2[H] \quad (2.2)$$

$$\frac{\partial[Q]}{\partial t} = -k_Q \cdot [Q] \cdot [H] + D_Q \nabla^2[Q] \quad (2.3)$$

where M is the inhibitor, k_a is the de-protection rate of inhibitor due to reaction with acid, Q is the base, k_Q is the neutralization rate between acid and base, D_H and D_Q are diffusion coefficients of the acid and base respectively.

3.2.3 Development model

The final step of the resist process is development. The development rate is a function of inhibitor concentration.

$$R = f([M]) \quad (3.1)$$

In general, the rate function is based on an empirical model (e.g., Mack development rate model) with its parameters obtained by fitting to experimental development rate or lithographic data [14].

Ultimately the development rate as a function of 3D spatial coordinates, $R(x, y, z)$, can be obtained when equations 1.1 to 3.1 are solved. Then the resist surface evolution can be computed by solving the following Eikonal equation that relates the arrival time, $T(x, y, z)$, to the development rate.

$$|\nabla T(x, y, z)| R(x, y, z) = 1 \quad (3.2)$$

The final resist profile is simply the surface defined by

$$T(x, y, z) = \text{development time} \quad (3.3)$$

3.2.4 Modeling of surface effects

Surface effects (e.g., surface contamination at top and/or bottom resist interface) sometime play an important role in determining resist top loss and/or bottom footing [20]. These effects may be modeled empirically by introducing a z-dependent scaling and/or addition to the initial acid distribution produced by exposure. For example, the z-dependent addition may be modeled by a function that reaches the maximum magnitude when z is at the resist surface and approaches zero when z is well inside the resist.

$$\Delta(z) \rightarrow \begin{cases} \Delta_{top} & z \rightarrow z_{top} \\ 0 & z \text{ well inside resist} \\ \Delta_{bot} & z \rightarrow z_{bot} \end{cases} \quad (4)$$

3.3 R3D model derivation

The formulation of R3D may be loosely characterized as a linear approximation to the 3D physical resist model. It consists of a series of terms that are linearly combined to approximate the resist processes. The expressions of these terms are determined by examining the analytical solutions to the physical resist model under some special conditions.

3.3.1 Initial acid generation

The exposure equations 1.1 and 1.2 can be easily solved assuming resist optical properties are independent of [PAG]. The initial acid concentration is therefore

$$[H_0] = 1 - e^{-C \cdot t_{exp} \cdot I} \approx C \cdot t_{exp} \cdot I \quad (5)$$

where t_{exp} is the exposure time. Note only the linear term of I is retained for the purpose of model simplification.

3.3.2 R3D formulation for PEB

The first PEB equation 2.1 can be solved similarly.

$$[M] = e^{-k_a \int [H] dt} \approx 1 - k_a \int [H] dt \quad (6.1)$$

In R3D, it may be more convenient to work with soluble concentration than inhibitor. It is defined as

$$[S] \equiv 1 - [M] \approx k_a \int [H] dt \quad (6.2)$$

Furthermore, taking a page from numerical methods, the integration can be approximated as a weighted sum of the acid at various time snapshot throughout the PEB process. It approaches the exact result when the snapshots are densely sampled in time.

$$[S] \approx \sum_{i=0}^N c_i [H(t_i)] \quad (6.3)$$

Eq. 6.3 is essentially the basic model form of R3D. Now we will solve the rest of the PEB equations that govern the acid and base diffusion/reaction under a few special conditions.

Condition I: Q=0

Under this condition, the PEB process reduces to a pure diffusion problem of acid.

$$\frac{\partial [H]}{\partial t} = D_H \nabla^2 [H] \quad (7.1)$$

This problem can be solved analytically for a planar resist film under the boundary condition of no acid loss through top or bottom resist surface. The solution at a given time, t_i , can be computed by applying a 3D Gaussian convolution to the initial acid distribution as shown in Eq. 7.2.

$$[H(t_i)] = [H_0] \otimes G(\sigma_i) \quad (i=0, 1, \dots, N) \quad (7.2)$$

The sigma of the Gaussian convolution kernel G is given as follows, also known as diffusion length.

$$\sigma_i = \sqrt{2D_H t_i} \quad (7.3)$$

Special care is required to handle the boundary condition at the resist top and bottom, which will be discussed in Section 3.4.3.

From equations 5, 6.3 and 7.2, we conclude that the R3D model needs to contain multiple optical image related terms, each represents the optical image convolved with a 3D Gaussian kernel of a sigma that corresponds to the diffusion length at different time snapshot.

Condition II: $k_q \rightarrow \infty$ and $D_H = D_Q = 0$

This condition means instant neutralization between acid and base, and there is no acid or base diffusion. The solution is

$$[H] = \max([H_0] - [Q_0], 0) \quad (8.1)$$

$$[Q] = \max([Q_0] - [H_0], 0) \quad (8.2)$$

where H_0 and Q_0 are initial acid and base distribution respectively.

Condition III: $k_q \rightarrow \infty$

This condition requires only instant neutralization between acid and base, but allows acid and base diffusion. It is a relaxed version of the condition II. The problem may be approximately solved in multiple time steps. At the beginning of each time step, the acid and base are neutralized instantly according to equations 8.1 and 8.2. Then for the rest of the time step, the acid and base are diffused independently, each can be solved using the same method as outlined in Condition I. The solution approaches the exact when the time step size Δt approaches zero.

$$[H(t_i)] = \max([H(t_{i-1})] - [Q(t_{i-1})], 0) \otimes G(\sigma_{D_H \Delta t}) \quad (9.1)$$

$$[Q(t_i)] = \max([Q(t_{i-1})] - [H(t_{i-1})], 0) \otimes G(\sigma_{D_Q \Delta t}) \quad (9.2)$$

Based on the above discussion, we also conclude that the R3D model needs to contain multiple terms related to $\max(I-b, 0)$ and $\max(b-I, 0)$, where b represents the effect of base, each convolved with a Gaussian kernel of a sigma that represents the diffusion length of acid or base at various time snapshot. Note although this model form is not the exact representation of the physical model, it does capture the main effects of acid/base neutralization and diffusion.

3.3.3 Surface effects

The surface effects in R3D can be modeled the exact same way as in Section 3.2.4 of the physical model. No simplification is required.

3.3.4 Development effect

Up to this point, R3D has finished calculation of Eq. 6.3, the soluble concentration. The next logical step would be converting it into development rate and solving the surface evolution problem of Eq. 3.2.

In this work we choose not to explicitly solve the development problem. Instead of taking a threshold on Eq. 3.3, we take a threshold on Eq. 6.3 to obtain the final resist profile. The development process may be considered as being implicitly modeled by model calibration. Note that the coefficients and the corresponding diffusion lengths in Eq. 6.3 need to be calibrated against experimental data. The development effects, which are embedded in the experimental data, are therefore effectively lumped into these model parameters. In addition, some of the development effects may be also modeled empirically by introducing a z-dependent threshold on Eq. 6.3.

3.3.5 Other effects

The R3D model may also contain additional terms to model other effects like flare, pattern loading and even etch effects. These are beyond the discussion of this work.

3.4 R3D implementation

All the essential terms required by the R3D model already exist in our 2D resist model except vertical diffusion and other z-dependent components such as acid scaling, addition and threshold. In this section, we discuss an efficient implementation of vertical diffusion. The implementation of other z-dependent components is straightforward.

It is important to note that the diffusion problem is mathematically separable in x, y and z coordinates, meaning that the 3D Gaussian convolution can be carried out separately as 1D Gaussian convolution in each of the x, y and z directions in any order and the final result stays the same. We choose to compute the diffusion in z direction first in R3D. We also choose to ignore the acid/base neutralization effect in the vertical diffusion step and let the horizontal diffusion step to take care of it. As a result, the calculation of vertical diffusion of chemical species boils down to the calculation of vertically-diffused optical image in light of the linear model (see Eq. 5).

3.4.1 3D optical image calculation

A 3D optical image is required for the vertical diffusion calculation, meaning 2D images in x-y plane need to be computed at multiple z locations in the resist. This increases runtime significantly as the total image computation time is proportional to the number of z locations. A fast method has been proposed in the past to speed up the calculation [15]. In this method, images in 3 planes are computed first and the image in an arbitrary plane can be obtained by quadratic interpolation. However, this method fails to capture standing wave effects. Complete absence of standing waves rarely happens in practice, even with well optimized bottom anti-reflection coating (BARC). This is because the reflectivity is angle dependent and it is nearly impossible to design a perfect BARC for all angles. In this section, we will derive a fast 3D image calculation method capable of modeling standing waves.

We start by decomposing the total electric field in resist into two fields.

$$\vec{E}(x, y, z) = \vec{E}_+(x, y, z) + \vec{E}_-(x, y, z) \quad (10)$$

where the two terms on the right-hand side represent the forward-propagating (FP) field, indicated by subscript “+”, and the backward-propagating (BP) field, indicated by subscript “-“, respectively. This decomposition is permitted due to the linear nature of Maxwell’s equations. Then the total field intensity can be written as.

$$I(x, y, z) \equiv |\vec{E}|^2 = I_A(x, y, z)[1 + B(x, y, z)] \quad (11.1)$$

$$I_A(x, y, z) \equiv |\vec{E}_+|^2 + |\vec{E}_-|^2 \quad (11.2)$$

$$B(x, y, z) \equiv \frac{2\text{Re}(\vec{E}_+ \cdot \vec{E}_-^*)}{|\vec{E}_+|^2 + |\vec{E}_-|^2} \quad (11.3)$$

where B represents the interference between the FP field and the BP field, which is the cause to standing waves, and I_A can be interpreted as the local average of I in z direction as the average smoothes out the standing wave. Although the above is derived for coherent images, it can be shown that the result applies to partially coherent images as well.

We now approximate the z-dependency of I_A using Lagrange polynomial as shown in equations 12.1 and 12.2. Other interpolation schemes may be used as well. Note second order polynomial (n=2) should provide good enough accuracy as the z-dependency is expected to be slow-varying without the standing wave.

$$I_A(x, y, z) \approx \sum_{i=0}^n I_A(x, y, z_i) w_i(z) \quad (12.1)$$

$$w_i(z) = \prod_{\substack{m=0 \\ m \neq i}}^n \frac{z - z_m}{z_i - z_m} \quad (12.2)$$

In addition, the interference factor B may be approximated by its open-frame value, which becomes pattern-independent. It can be readily computed once the exposure optics and wafer film stack information become available.

$$B(x, y, z) \approx B(z) \quad (13)$$

From equations 11.1, 12.1 and 13, the 3D image is approximated as follows.

$$I(x, y, z) \approx \sum_{i=0}^n I_A(x, y, z_i) w_i(z) [1 + B(z)] \quad (14.1)$$

An alternative approximation to Eq. 14.1 may be given by following equation.

$$I(x, y, z) \approx \sum_{i=0}^n I(x, y, z_i) f_i(z) \quad (14.2)$$

$$f_i(z) \equiv w_i(z) [1 + B(z)] / [1 + B(z_i)] \quad (14.3)$$

Eq. 14.2 has the property that the image is exact at the sample locations $z=z_i$. Note the properties of Eqs. 11.1 and 13 are used in deriving Eq. 14.2 from Eq. 14.1.

Unlike the fast method in prior work [15], this new fast method is capable of modeling stand wave effects with three sampling planes. Fig.4 shows the comparison of 3D optical images computed by the rigorous method and the new fast method. In the rigorous method, the image at a given z -location is computed rigorously, while in the fast method it is “interpolated” from the images at the top, middle and bottom of the resist based on Eqs. 14.2 & 14.3. In the simulations the BARC layer properties were varied to produce different amount of reflection, characterized by R , defined as the energy ratio of the backward-propagating field to the forward-propagating field. The standing wave effects are clearly visible in these images, even with R as low as 0.07%. The standing wave effects are captured very well by the fast method of this work.

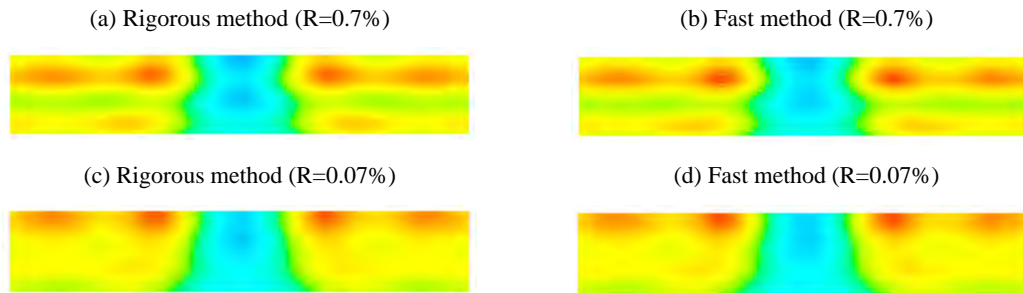


Fig. 4. Comparison of 3D optical images computed by rigorous method and fast method. In the rigorous method, the image at a given z location is computed rigorously (a, c). In the fast method, the image at a given z location is “interpolated” from images at the top, middle and bottom of the resist (b, d). R is the energy ratio of the backward-propagating field to the forward-propagating field.

3.4.2 Vertical diffusion calculation

Equation 14.1 or 14.2 offers a convenient way to pre-compute the diffusion. Using Eq. 14.2 as an example, the z-diffused image is given by

$$\tilde{I}(x, y, z) = \sum_{i=0}^n I(x, y, z_i) \tilde{f}_i(z) \quad (15.1)$$

$$\tilde{f}_i(z) = f_i(z) \otimes G_z \quad (15.2)$$

where G_z is a 1D Gaussian convolution kernel in z direction, and “~” denotes a z-diffused quantity. Note that the z-diffused image is a weighted sum of optical images sampled at $z=z_i$. The weighting factors can be pre-computed and is pattern-independent.

3.4.3 Boundary condition

When carrying out the convolution in Eq. 15.2, one needs to properly handle the boundary condition at the resist top and bottom. Note the analytical solution to the diffusion problem of Eq. 7.1 is given by

$$H(x, y, z, t) = \sum_l a_l(x, y, t) \cos\left(\frac{\pi l}{L_z} z\right) e^{-D_H \left(\frac{\pi l}{L_z}\right)^2 t} \quad (16)$$

where a_l is Fourier cosine transform of H in z direction, L_z is the resist thickness. This solution form indicates that the calculation domain can be extended periodically by taking the mirror image of the original with respect to the resist top and bottom, which enables diffusion calculation via Gaussian convolution.

3.4.4 Diffused TCC approach

The vertical diffusion effects can be incorporated into TCC, resulting in a so-called diffused TCC. It can be derived by placing I in Eq. 15.1 with TCC.

$$T\tilde{C}C(\vec{k}', \vec{k}'', z) = \sum_{i=0}^n TCC(\vec{k}', \vec{k}'', z_i) \tilde{f}_i(z) \quad (17)$$

This approach offers the advantage of no runtime impact in OPC and verification applications. Although it will slow down TCC generation, the impact is minimized to the calculation of only a few nearby optical TCCs ($n=2$ should be enough) using the approach developed in Section 3.4.1.

3.4.5 Other considerations

The approach developed in Section 3.4.1 for 3D optical image calculations, where a 3D distribution is decomposed into products of 2D distribution in x-y plane and 1D distribution in z direction, may be extended to calculations of other resist properties such as soluble concentration. Better accuracy may be expected since resist processes generally reduce standing wave effects significantly. It provides a quick calculation of resist profile at any z location.

3.5 R3D validation against physical resist model

We now present a benchmark study of the R3D model against the 3D physical resist model. The R3D simulations were done on Brion's Tachyon computational lithography platform [18]. The physical resist model simulations were carried out using the commercial lithography simulation software Prolith [19]. The procedure is as follows. (1) First, the 3D physical resist model was used to generate the reference data, which consists of resist CDs of about 200 line/space patterns of various pitches and widths, as well as 2D end-to-end (ETE) and contact patterns, measured at 20 z-locations throughout the resist thickness, under 9 defocus conditions. (2) Then, a small subset of the reference data was used to calibrate the R3D model. (3) Finally, resist CDs at all 20 z-locations under all 9 defocus conditions as in (1) were simulated using the calibrated R3D model. The resist profiles were constructed using these CDs and compared between the R3D model and the 3D physical resist model.

3.5.1 3D physical resist model simulation

Two flavors of the 3D physical resist model were used in this study. One is a generic CAR model with all the resist effects as described in Section 3.2 except for surface effects, and the other is the same as the first one but with a surface contamination at the resist top.

Examples of the simulated resist profiles using the 3D physical resist model are shown in Fig. 5. Note there are big differences between the resist profiles after development and the initial optical image contours, indicating there are strong resist effects in these physical models. The optical image contours were obtained by taking a constant threshold on the optical images. The optical images are shown as color maps in Fig. 5. The threshold was determined by anchoring the image CD to resist CD for the 1D feature of pitch=110nm and width=55nm at resist height=15nm.

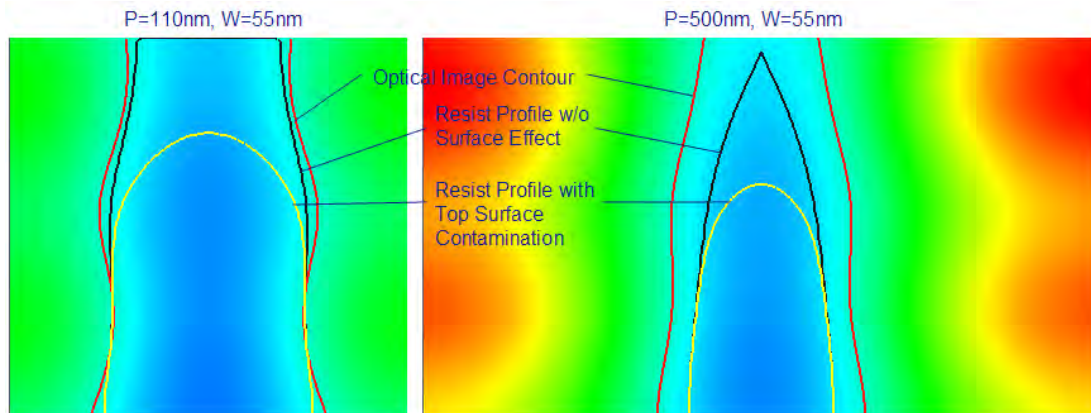


Fig. 5. Examples of resist profiles simulated by the 3D physical resist model.

3.5.2 R3D model calibration

A small subset of the reference data, which consists of CDs of only 1D patterns at 3 z-locations under 3 defocus conditions, was used to calibrate the R3D model. The fitting RMS's are shown in Table 1.

Table 1. R3D fitting RMS

Model w/o surface effect	Model with top surface contamination
0.93 nm	1.5 nm

3.5.3 R3D prediction of resist profiles

The calibrated R3D model was then used to predict resist CDs at all z-locations under all defocus conditions as used in the physical resist model simulations. The through-focus resist sidewall profiles of 55nm line at selected pitches predicted by R3D are compared with those of the 3D physical resist model in Figure 6 for the model with no surface effects, and in Figure 7 for the model with top surface contamination. Good agreement is found between the R3D model and the 3D physical resist model. Comparisons of other line widths also show the similar conclusion. The through-focus resist profiles of 2D patterns predicted by R3D are shown in Figure 8 and Figure 9 for ETE and contact patterns respectively. Although the R3D model was calibrated using only bright-field 1D patterns, it showed good prediction capability for both bright-field and dark-field 2D patterns too. These results indicate that the physical nature of the original physical resist model is largely retained in the R3D model.

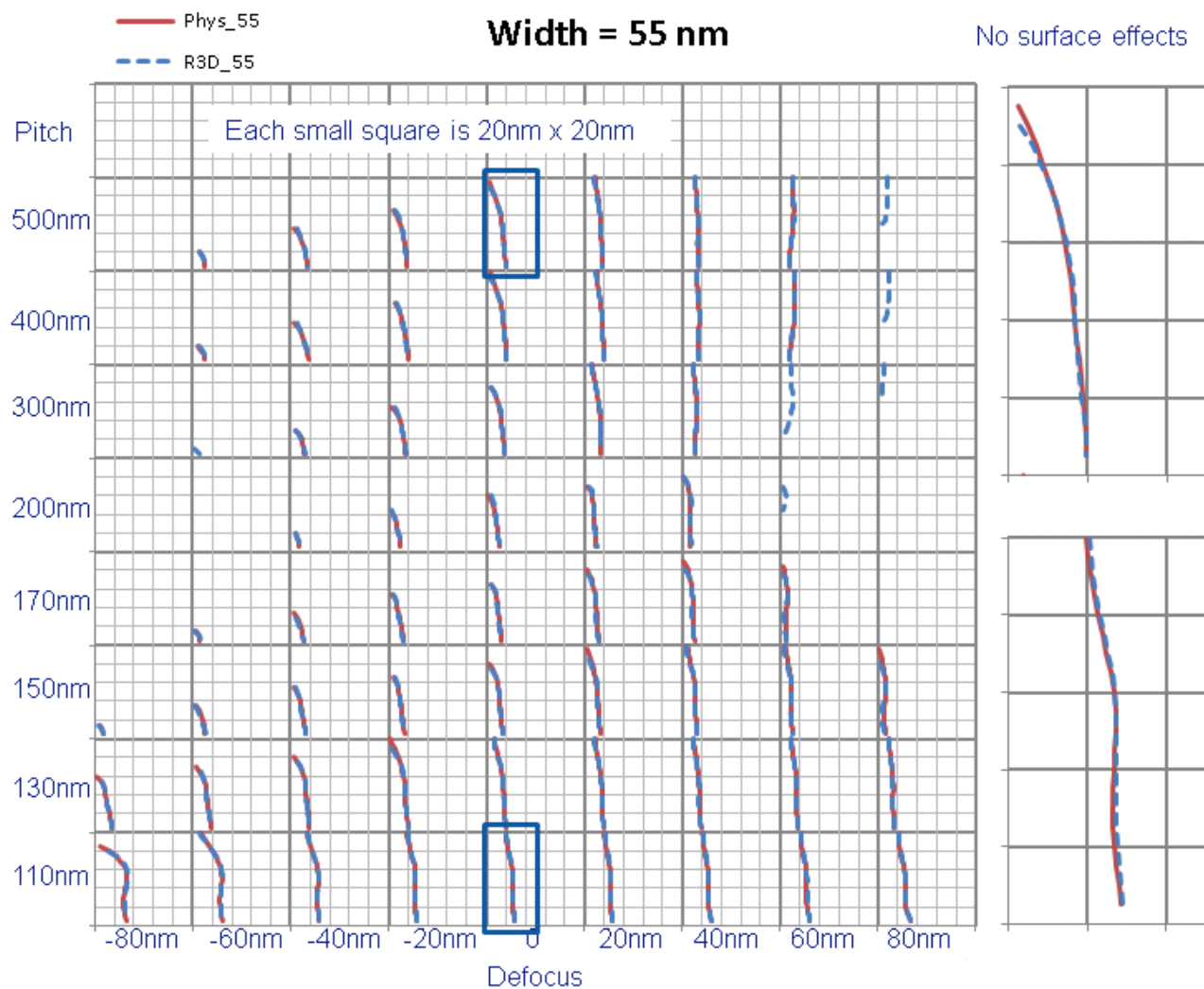


Fig. 6. Comparison of resist sidewall profiles (only right side is plotted) between R3D and 3D physical resist model with no surface effects. Each small square is 20nm by 20nm in size. Each big box corresponds to one defocus condition labeled on the very bottom and one pitch condition labeled on the far left side. Two enlarged views of pitch=500nm and pitch=110nm under the nominal focus condition are shown on the right.

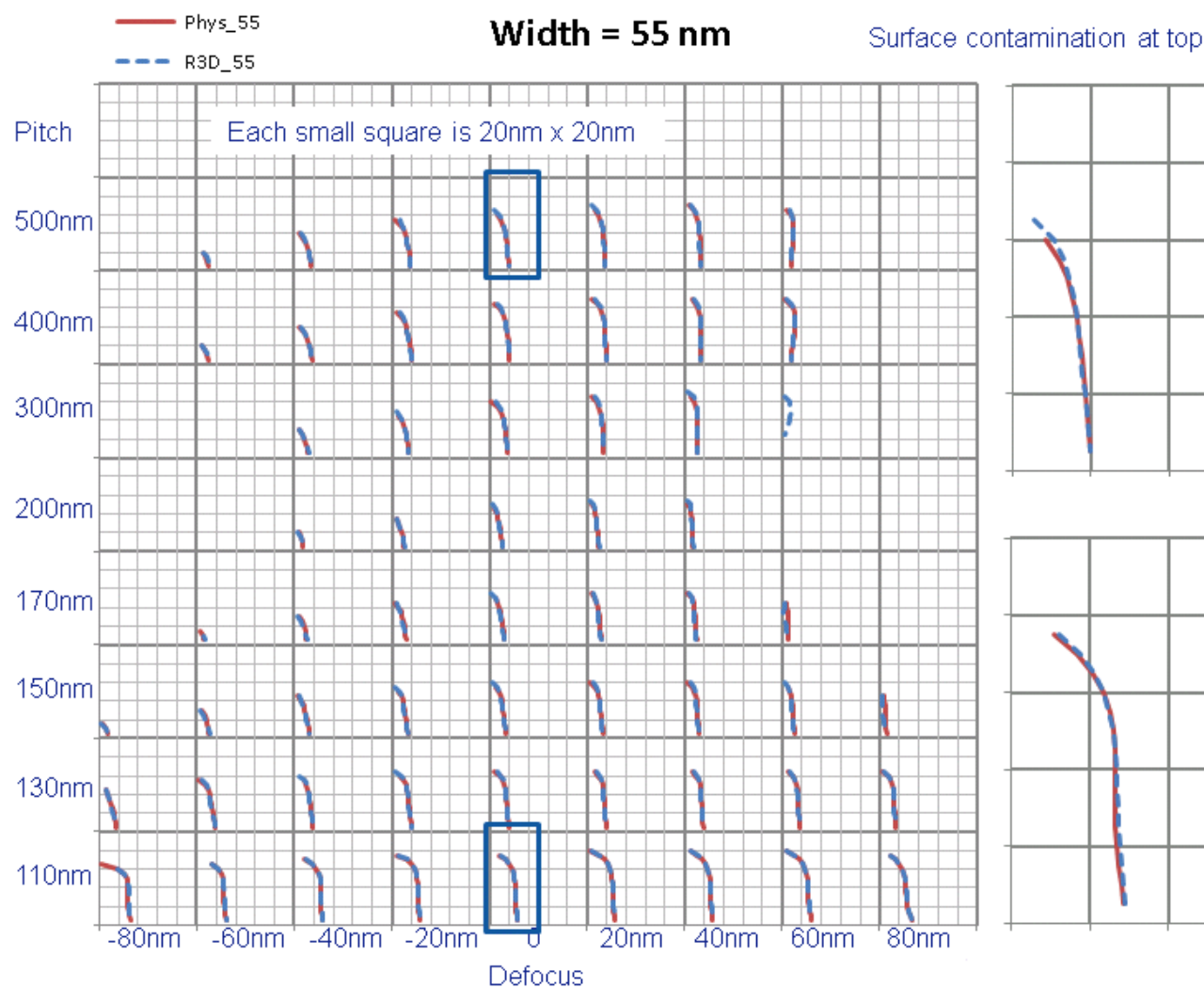


Fig. 7. Comparison of resist sidewall profiles (only right side is plotted) between R3D and 3D physical resist model with surface contamination at top. Each small square is 20nm by 20nm in size. Each big box corresponds to one defocus condition labeled on the very bottom and one pitch condition labeled on the far left side. Two enlarged views of pitch=500nm and pitch=110nm under the nominal focus condition are shown on the right.

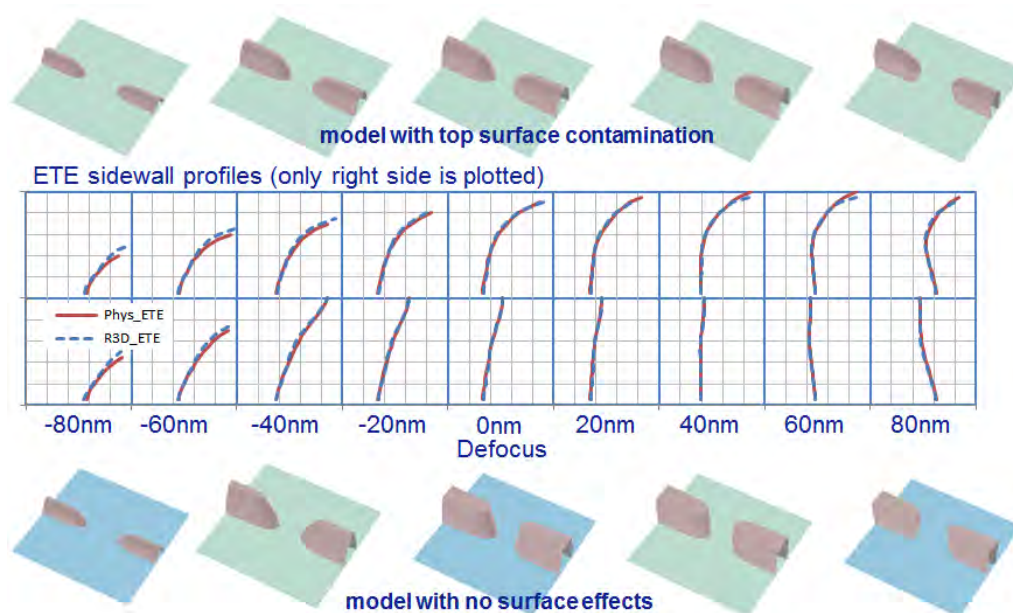


Fig. 8. Comparison of through-focus ETE resist sidewall profiles (only right side is plotted) between R3D and 3D physical resist model. Each small square is 20nm by 20nm in size. Each big box corresponds to one defocus condition labeled on the bottom. The upper half shows the profiles for the resist model with surface contamination at top. The lower half shows the profiles for the resist model without surface effects.

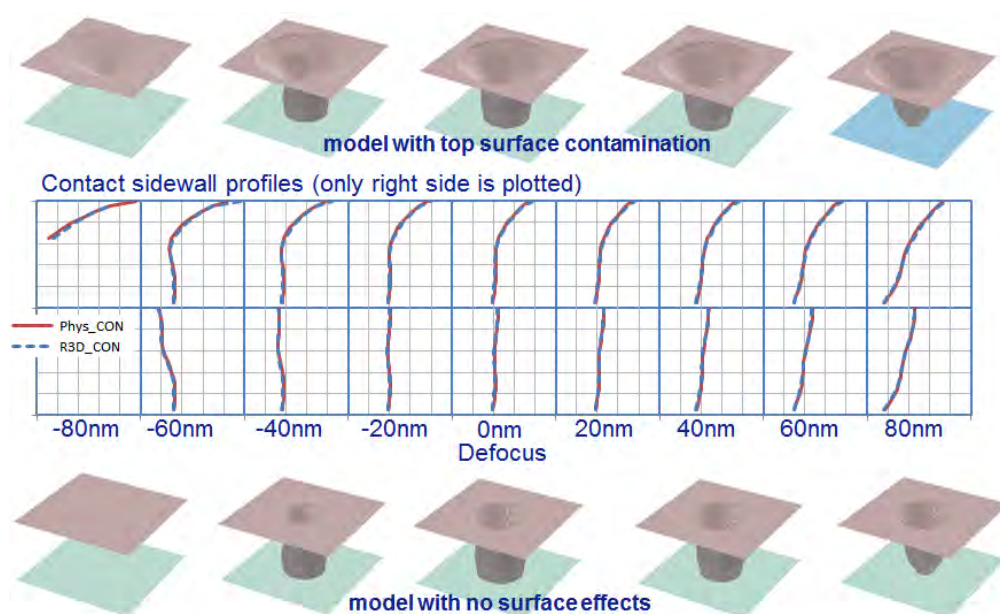


Fig. 9. Comparison of through-focus contact resist sidewall profiles (only right side is plotted) between R3D and 3D physical resist model. Each small square is 20nm by 20nm in size. Each big box corresponds to one defocus condition labeled on the bottom. The upper half shows the profiles for the resist model with surface contamination at top. The lower half shows the profiles for the resist model without surface effects.

4. W3D

Although underlying wafer topography always exists in a typical semiconductor lithography process except for the first layer, its effects are generally ignored in critical layers such as poly and contact layers where BARC is usually used and in non-critical layers such as implant layers where features sizes are large. However, this practice starts to hit its limit as the device feature sizes continue to shrink. The impact of wafer topography in a double-patterning process due to the first lithography step has been reported to reduce the process window of the second lithography step [9]. Studies have also shown that OPC is required to correct the problem of severe image distortions caused by wafer topography in implant processes [8]. Although wafer topography effects can be simulated using rigorous EMF models, the computational cost is prohibitive for full-chip applications. We have developed fast, approximate models for full-chip applications. One is a kernel based empirical model. The details of this model are given elsewhere [10]. In this section, we present the development of a more physical Tachyon W3D model and the preliminary results against rigorous simulations.

4.1 W3D model form

The lithography process with wafer topography is a double-diffraction process in series, in which the diffracted light by the mask is diffracted again by the wafer topography. Let's first consider a coherent incident field onto the wafer surface plane produced by the mask. The incident field in the plane can be expressed as a Fourier expansion in which each Fourier component represents a plane wave.

$$\vec{E}_{inc}(\vec{x}) = \sum_{\vec{k}} \vec{E}_{\vec{k}} e^{i\vec{k} \cdot \vec{x}} \quad (18)$$

where $\vec{x} = (x, y)$ denotes the spatial coordinates in the x-y plane, $\vec{k} = (k_x, k_y)$ denotes the plane wave wave vector projection in the x-y plane, and $\vec{E}_{\vec{k}}$ is the polarization of the plane wave. Each of the plane waves is diffracted by the underlying wafer topography, a process very similar to the mask diffraction. The field in the resist film can be written as follows.

$$\vec{E}(\vec{x}, z) = \sum_{\vec{q}, \vec{k}} \vec{W}_{\vec{q}, \vec{k}}(z) \cdot \vec{E}_{\vec{k}} e^{i(\vec{q} + \vec{k}) \cdot \vec{x}} \quad (19)$$

where \vec{W} is a tensor that models light propagation in the wafer film stack and can be computed via rigorous simulations. It is defined as the ratio of a diffracted Fourier polarization component to an incident plane wave polarization component. One Fourier component in the resist film actually consists of two plane waves, one propagates forward and the other propagates backward.

To separate out the topography effect, it is useful to re-write Eq. 19 in the following form.

$$\vec{W}_{\vec{q}, \vec{k}}(z) = \delta_{\vec{q}, 0} \vec{W}_{\vec{k}}(z) + \vec{S}_{\vec{q}, \vec{k}}(z) \quad (20)$$

where the first term is the portion of the 0th diffraction order (i.e., $\vec{q} = 0$) that represents the planar film stack effect, and the second term, we call it topography function in this work, models the scattering effect from the underlying topography. Now we make the following approximation, which assumes the topography function is independent of incident angle.

$$\vec{S}_{\vec{q}, \vec{k}}(z) \approx \vec{S}_{\vec{q}}(z) \quad (21)$$

Note this approximation is analogous to Hopkins treatment of oblique incidence in mask diffraction. Substituting Eqs. 20 and 21 into Eq. 19, we obtain the following field in resist film.

$$\vec{E}(\vec{x}, z) \approx \vec{E}_0(\vec{x}, z) + \vec{S}(\vec{x}, z) \cdot \vec{E}_{inc}(\vec{x}) \quad (22.1)$$

$$\vec{E}_0(\vec{x}, z) = \sum_{\vec{k}} \vec{W}_{\vec{k}}(z) \cdot \vec{E}_{\vec{k}} e^{i\vec{k} \cdot \vec{x}} \quad (22.2)$$

$$\vec{S}(\vec{x}, z) = \sum_{\vec{q}} \vec{S}_{\vec{q}}(z) e^{i\vec{q} \cdot \vec{x}} \quad (22.3)$$

In Eq. 22.1, the first term (or Eq. 22.2) is simply the field produced by the planar film stack and the second term is the scattered field produced by the underlying topography. The optical image intensity is given by.

$$I = \left| \vec{E}_0 + \vec{S} \cdot \vec{E}_{inc} \right|^2 \quad (23)$$

Unfortunately the fields in Eq. 23 are not directly available in OPC and verification applications in which Hopkins TCC image models are used. Only image intensities in the planar wafer film stack are computed by a TCC image model. We need to make additional approximations to estimate the field from the intensity. Based on Eq. 23, we construct our W3D model form as follows.

$$I = \sum_{\alpha=x,y,z} \left| \sqrt{I_{0\alpha}} + \sum_{\beta=x,y,z} S_{\alpha\beta} \sqrt{I_{inc,\beta}} \right|^2 \quad (24)$$

where I_{0x} , I_{0y} and I_{0z} are planar wafer image intensity components in x, y, z directions respectively, $I_{inc,x}$, $I_{inc,y}$ and $I_{inc,z}$ are incident field image intensity components in x, y, z directions respectively. The distribution of each component in the total intensity may be estimated from the source shape and polarization. Although Eq. 24 is constructed based on the analysis of coherent image, we will use the same model form for partially coherent image as well. This model form is self-consistent in the sense that it reduces to planar wafer solution when there is no underlying wafer topography, i.e., the topography function $S = 0$.

4.2 Calculation of topography function

From Equations 19 to 21, the topography function can be obtained from the field produced by an incident plane wave. Although a rigorous EMF solver can be used to compute the field, it is impractical for full-chip application. In this work, we adopt the methodology developed in Section 2 to compute the topography function.

Following a similar procedure as outlined in Fig.2 of Section 2, we first run rigorous simulations to compute the fields produced by representative wafer topography elements and extract the so-called W3D filters from these fields. Then these filters can be re-used to render the topography function of an arbitrary underlying topography pattern using a similar procedure as described in Fig. 1 of Section 2. The main differences would be replacing the mask pattern and topography with the underlying wafer pattern and topography, subtracting the planar wafer field, and properly taking into account the phase difference between the scattered field and the planar wafer field.

4.3 Estimation of incident field image

Assuming that planar wafer image intensity I_0 is available, then the last piece of information we need is the estimation of the incident field intensity in Eq. 24 in order to compute the non-planar wafer image. One method is using the average intensity as discussed in Section 3.4.1. From Eqs. 11.1 and 13, we obtain

$$I_{inc} \approx I_0 / (1 + B) \quad (25)$$

The average intensity removes the standing wave caused by the interference between the incident field and the reflected field, and is therefore expected to be more representative to the incident field intensity than the total intensity. We may

also introduce a more sophisticated estimation with a convolution to account for the profile differences between the incident field intensity and the average intensity.

$$I_{inc} \approx I_0 \otimes K / (1 + B) \quad (26)$$

The functional form of the convolution kernel K may be constructed from rigorous simulations of typical features and/or calibrated to experimental data.

4.4 Proof-of-concept evaluation

In this section we present a proof-of-concept evaluation of W3D on an implant process. The mask and wafer configuration is shown in Figure 10. The wafer topography beneath the resist film consists of active areas, labeled as Rx in the figure, separated by shallow trench isolation (STI) areas. The planar film stack corresponds to areas where there are no Rx structures. The mask is designed to block the exposure of the Rx areas in an alternating fashion.

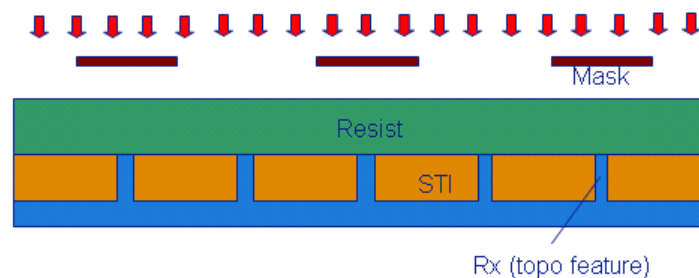


Fig. 10. Mask and wafer configuration used in the proof-of-concept evaluation of W3D. The planar film stack corresponds to the condition of no active structures (labeled as Rx in the figure).

The wafer exposure was simulated using a rigorous EMF solver based on a Finite Difference Time Domain (FDTD) method in both planar and non-planar areas. The mask was convolved with a low-pass filter to mimic the lens projection process. Un-polarized source was assumed in this implant process, therefore the total image was obtained as an average of x- and y-polarized images. The planar wafer images were used by the W3D model to compute the non-planar wafer images according to Eqs. 24 and 25. In both FDTD and W3D simulations, the final optical images were convolved with a Gaussian kernel to mimic the resist process. Then the resist CDs were computed by applying a constant threshold to the diffused images.

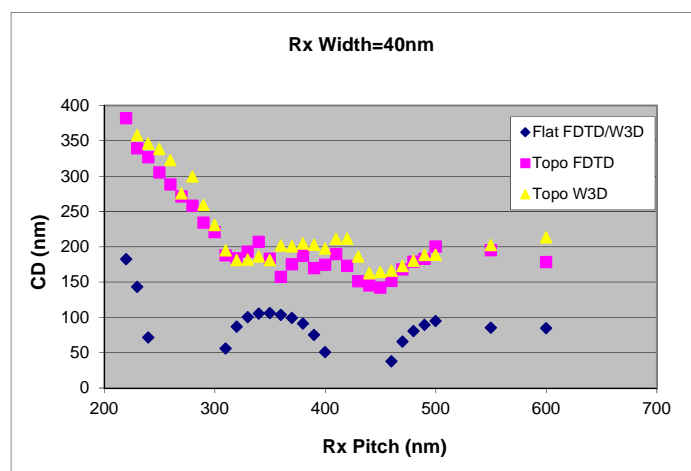


Fig. 11. CD comparison between W3D and FDTD simulations. By design, W3D and FDTD produce the same result in the planar (flat) area.

Figure 11 shows the through-pitch implant resist CDs in planar (flat) and non-planar (topo) areas obtained by FDTD and W3D simulations. By design (see Eq. 24), FDTD and W3D produce the same result in planar areas. As one can see, the underlying topography induced CD difference is quite significant between planar and non-planar areas. The majority of the topography effect is clearly captured by the W3D model. This is a very promising result considering the fact that there are no adjustable parameters or calibrations involved in this proof-of-concept evaluation. Additional improvements may be expected once we finish implementing the method of Eq. 26.

4.5 Future work

We are in process of implementing Eq. 26 and integrating the W3D model into our model generation/calibration as well as OPC and verification simulation flows. The progress and accuracy benchmark studies will be reported in our future work.

5. SUMMARY

We have presented a full-chip 3D computational lithography framework. It consists of three fast models (namely Tachyon M3D, R3D and W3D) that are capable of accurate prediction of 3D lithography effects in all lithography processes which include 3D mask topography, 3D resist profile and 3D wafer topography effects. The working principle and accuracy validation of Tachyon M3D have been discussed in our previous work and are reviewed in this work for completeness. The development of Tachyon R3D and its benchmark against 3D physical resist models have been described in great details in this work. Finally we have shown the development of Tachyon W3D and its proof-of-concept evaluation against rigorous simulations. Implementation of W3D in production flows is in process.

ACKNOWLEDGEMENTS

The authors would like to thank Steve Hansen for providing a base 3D lithography model and assistance in some of the Prolith simulations. The authors also would like to thank Martin Snajdr for creating very useful scripts for data analysis automation.

REFERENCES

- [1] Christophe Pierrat, Alfred Wong, Sheila Vaidya, Matthew Vernon, "Phase-Shifting Mask Topography Effects on Lithographic Image Quality," 28 / SPIE Vol. 1927 Optical/Laser Microlithography VI (1993)
- [2] Kevin D. Lucas, Andrzej J. Strojwas, K. K. Low, Chi-Min Yuan, "Intensity Optimization for Phase Shifting Masks," 438 / SPIE Vol. 1927 Optical/Laser Microlithography VI (1993)
- [3] Frank Staals et al., "Advanced Wavefront Engineering for Improved Imaging and Overlay Applications on a 1.35 NA Immersion Scanner," Proc. of SPIE Vol. 7973, 2011
- [4] Jo Finders and Thijs Hollink, "Mask 3D effects: impact on Imaging and Placement," 27th European Mask and Lithography Conference, Proc. of SPIE Vol. 7985, 2011
- [5] Peng Liu, "Accurate prediction of 3D mask topography induced best focus variation in full-chip photolithography applications," Proc. of SPIE Vol. 8166, 816640 (2011)
- [6] Chandra Sarma et al., "3D physical modeling for patterning process development," Proc. of SPIE Vol. 7641, 76410B (2010)
- [7] Mohamed Talbi et al., "Three-dimensional physical photoresist model calibration and profile-based pattern verification," Proc. of SPIE Vol. 7640, 76401D (2010)
- [8] Dongbing Shao et al., "Substrate Aware OPC Rules for Edge Effect in Block Levels," Proc. of SPIE Vol. 7823, 78233U (2010)
- [9] Itaru Kamohara and Thomas Schmoeller, "Split, overlap, stitching, and process design for double patterning considering local reflectivity variation by using rigorous three-dimensional wafer-topography and lithography simulation," J. Micro/Nanolith. MEMS MOEMS 10(2), 023013 (Apr-Jun 2011)

- [10] Peng Liu et al, "Fast and accurate 3D mask model for full-chip OPC and verification," Proc. of SPIE Vol. 6520, 65200R, (2007)
- [11] Jeffrey Byers, John Petersen, John Sturtevant, "Calibration of Chemically Amplified Resist Models," Proc. SPIE 2724, 156 (1996)
- [12] Ebo Croffie1, Mosong Cheng, Andrew Neureuther, "Modeling Chemically-amplified Resists for 193nm Lithography," Proceedings of SPIE Vol. 3999 (2000)
- [13] Andreas Erdmann, Tim Fühner, Feng Shao, and Peter Evanschitzky, "Lithography Simulation: Modeling Techniques and Selected Applications," Proc. of SPIE Vol. 7390, 739002 (2009)
- [14] Stewart Robertson, Chris Mack and Mark Maslow, "Towards a Universal Resist Dissolution Model for Lithography Simulation," Proceedings of SPIE Vol. 4404 (2001)
- [15] Jeffrey Byers, Mark Smith, and Chris Mack, "3D Lumped Parameter Model for Lithographic Simulations," Proceedings of SPIE Vol. 4691 (2002)
- [16] Songyi Park et al., "Model based OPC for implant layer patterning considering wafer topography proximity (W3D) effects," To be presented to SPIE Advanced Lithography 2012
- [17] F. H. Dill, W. P. Hornberger, P. S. Hauge, and J. M. Shaw, "Characterization of positive photoresist," IEEE Trans. Electron Devices 22, 445–452 (1975)
- [18] <http://www.brion.com>
- [19] <http://www.kla-tencor.com/lithography-modeling/chip-prolith.html>
- [20] Chris A. Mack, "Fundamental Principles of Optical Lithography: The Science of Microfabrication," John Wiley & Sons, London (2007)